The Impact of Simplifications on the Performance of a Finite Element Model of a *Macaca fascicularis* Cranium

LAURA C. FITTON,[1]* MIGUEL PRÔA,[1] CHARLIE ROWLAND,[1] VIVIANA TORO-IBACACHE,[1,2] AND PAUL O'HIGGINS[1]

[1]Centre for Anatomical and Human Sciences, Department of Archaeology and Hull York Medical School, University of York, York, United Kingdom

[2]Facultad de Odontología, Universidad de Chile, Santiago, Chile

ABSTRACT

In recent years finite element analysis (FEA) has emerged as a useful tool for the analysis of skeletal form-function relationships. While this approach has obvious appeal for the study of fossil specimens, such material is often fragmentary with disrupted internal architecture and can contain matrix that leads to errors in accurate segmentation. Here we examine the effects of varying the detail of segmentation and material properties of teeth on the performance of a finite element model of a *Macaca fascicularis* cranium within a comparative functional framework. Cranial deformations were compared using strain maps to assess differences in strain contours and Procrustes size and shape analyses, from geometric morphometrics, were employed to compare large scale deformations. We show that a macaque model subjected to biting can be made solid, and teeth altered in material properties, with minimal impact on large scale modes of deformation. The models clustered tightly by bite point rather than by modeling simplification approach, and fell out as being distinct from another species. However localized fluctuations in predicted strain magnitudes were recorded with different modeling approaches, particularly over the alveolar region. This study indicates that, while any model simplification should be undertaken with care and attention to its effects, future applications of FEA to fossils with unknown internal architecture may produce reliable results with regard to general modes of deformation, even when detail of internal bone architecture cannot be reliably modeled. Anat Rec, 298:107–121, 2015. © 2014 Wiley Periodicals, Inc.

Key words: fossil hominins; virtual reconstruction; sensitivity study; model building; cranial deformation; Procrustes size and shape analysis; finite element analysis; geometric morphometrics

Computed tomography (CT) is now frequently used for the imaging of fossils, facilitating noninvasive studies of internal morphology and enabling three-dimensional virtual reconstruction (Gunz et al., 2009; Benazzi et al., 2011; Grine et al., 2012; Benazzi et al., 2014). Once created, these virtual models can be used in morphological and functional simulations, such as finite element analysis (FEA), a method that predicts how an object deforms with applied loads and constraints. How specimens respond to different loading regimens may be indicative
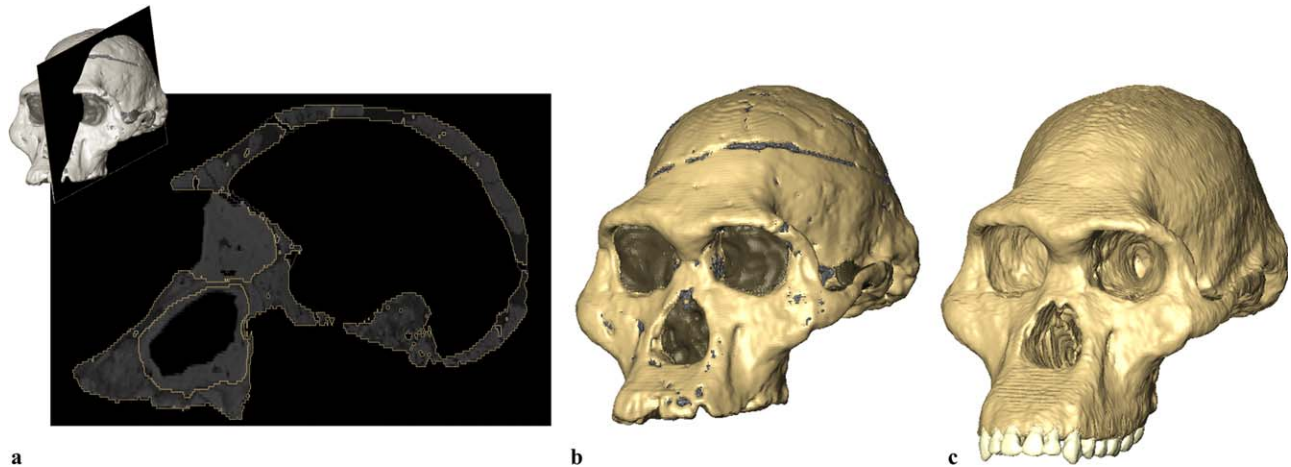
Fig. 1. (**a**) Computed tomography (CT) slice through a surface segmentation of Sts5 (*Australopithecus africanus*). Bone, air, and the sediment matrix have been segmented into different materials. Note the varying density levels (gray scale) throughout the slice, the presence of matrix in the maxillary sinus and orbit, and lack of detail of cancellous bone and cracks in the specimen. (**b**) Surface rendering of Sts5 following an initial stage of reconstruction (cream = bone; gray = cracks manually filled in; brown = sediment matrix). Cracks have been manually filled. (**c**) The final stage of CT reconstruction; sediment has been removed, cracks replaced with solid cancellous bone and the alveolar margin and dentition of Sts5 reconstructed using a scaled and transformed maxilla and the dentition of another *A. africanus* specimen (Sts52).

of behaviors experienced during life and is more frequently used to predict behaviors, such as feeding, and diet (Dumont et al., 2005; Macho et al., 2005; McHenry et al., 2006; Wroe et al., 2007; Jasinoski et al., 2009; Strait et al., 2009, 2010; Wroe et al., 2010; Dumont et al., 2011; Cox et al., 2012; Strait et al., 2013). The underlying rationale behind using FEA to elucidate diet is that by loading a specimen in different ways and assessing which scenarios an individual is more or less able to resist, mechanical loading history and evolutionary functional adaptations may be inferred. Since different feeding behaviors require and produce different masticatory system loadings, and are directly related to food mechanical and material properties, FEA has obvious appeal in studies of extinct specimens.

Bone deforms under a given load, but the extent and manner in which it deforms depend on several factors, including the bone's material properties, how the specimen is loaded, and the specimen's internal and external morphology. These various factors pose a problem when simulating biting in fossil specimens because reconstructing the bony morphology of fossils is often not straightforward. CT scans can capture the internal and external morphology of bone; however, fossils are usually discovered distorted, broken, fragmentary, and filled with matrix, leading to difficulty in fully reconstructing external and internal morphology.

Three-dimensional visualization software can be used to piece together fossil fragments, separate the fossil from the surrounding matrix, replace missing parts, and correct distortions (Gunz et al., 2009; Strait et al., 2009; Benazzi et al., 2011; Grine et al., 2012; Benazzi et al., 2014). The first step in virtual fossil reconstruction is to segment the bone from the surrounding air, spaces, and matrix. By identifying scan grey-level differences between these components, the boundaries can be outlined via thresholding, and thus segmented into different materials (Fig. 1a). However, sedimentary matrix

may have a density smaller or greater than the fossil bone itself, which makes automatic thresholding problematic. Matrix can be found in regions such as the orbits, nasal cavity, temporal fossae and internally in the sinuses, as in the case of the well-known *Australopithecus africanus* cranium (Sts5) (Fig. 1a,b). The thickness of bone in these matrix-affected regions can easily be over- or under-estimated during the reconstruction process (Fig. 1c). Smaller cavities like those found in regions of trabecular bone, foramina, and air cells may also be filled, or the CT scan itself may lack detail at the low resolution typical of clinical scanners. Owing to time constraints and some of the problems noted above, even virtual models of extant species are often approximated. For instance, complex and thin bony structures, such as the nasal conchae are commonly simplified or ignored (Dumont et al., 2005; Strait et al., 2005, 2007, 2009; Chalk et al., 2011), and trabecular bone is simplified, often being modeled as a solid volume (Strait et al., 2009) or with just the larger trabecular struts represented but modeled with the material properties of cortical bone (Kupczik et al., 2009; Fitton et al., 2012). Thus, even if best efforts are made to virtually reconstruct individuals it is not possible to ensure reconstructions accurately reflect the original internal architecture of the individual.

Finite element (FE) models of fossil hominins have obvious appeal (Strait et al., 2009; Wroe et al., 2010), but these models will undoubtedly contain artifacts in the form of simplifications and solidifications to a greater or lesser extent. So, how reliable are the resulting FE models given the large number of errors that may be introduced during the reconstruction process? The sensitivity of cranial finite element analyses to variations in input parameters such as muscle force (Ross et al., 2005; Fitton et al., 2012), muscle orientation (Cox et al., 2011), bone material properties (Kupczik et al., 2007; Cox et al., 2011), the representation of periodontal

ligament (Wood et al., 2011), and cranial sutures (Kupczik et al., 2007; Wang et al., 2010; Bright, 2012; Wang et al., 2012) has previously been examined. The results of these studies have highlighted the different impacts that such assumptions and simplifications can have on FE model performance, yet the consequences of simplifications in model reconstruction and building have not yet been fully examined and need to be further understood.

An additional aspect of model simplification that requires investigation concerns the teeth. In order to properly represent the teeth they need to be segmented in detail from the surrounding bone and modeled with differing material properties for enamel and dentine. First, a potential issue arises because the teeth are not continuous with surrounding bone but are separated by the periodontal ligament (PDL) which, although thin, may be important in relation to model performance. This issue has been addressed previously by Wood et al. (2011) in the cranium, who found the PDL, represented as a layer of low modulus material between teeth and bone, to have little effect except on local strains; however, the situation appears to be different in FE models of the mandible (Gröning et al., 2011), where a significant increase in local and global deformation arose with the introduction of a similar layer representing PDL. Teeth are themselves composed of a number of materials including dentine and enamel. How to model teeth accurately therefore creates a whole challenge in itself (Macho et al., 2005; Benazzi et al., 2012), since roots are principally dentine which has a similar Young's modulus to bone under compression (bone: 17 GPa, Ashman and van Buskirk 1987; Dechow et al., 1993; dentine: 20–25 GPa; Kinney et al., 2003) while enamel has a highly variable (depending on orientation and location) yet higher elastic modulus of 50–120 GPa (Cuy et al., 2002). An alternative strategy is to ignore the difference between teeth and bone and simply model the teeth as having the same material properties as surrounding bone. In such a solid model the tooth roots would be indistinguishable from surrounding bone. Whilst the effects of such manipulations are unknown, the modeling of teeth using the material properties of bone is a common practice (Strait et al., 2005; Wroe et al., 2007; Kupczik et al., 2009; Wang et al., 2010, Gröning et al., 2011; Fitton et al., 2012). Another strategy is to model the teeth with the material properties of enamel, which is much stiffer than bone (Strait et al., 2009; Cox et al., 2011). The effects of these modeling simplifications on FE predictions of cranial performance during biting are poorly understood and form the basis of the present study.

We employ a macaque cranial model that has already formed the basis of a number of investigations, including validation using strain gauges (Kupczik et al., 2007) and sensitivity studies examining the effect of masticatory loading, sutures and material properties on FE model performance (Kupczik et al., 2007; Fitton et al., 2012). Here validation is not addressed further. Rather, the aim is to investigate the sensitivity of FE results to some assumptions made during the reconstruction stage of model building. A series of models with progressively filled internal cavities, and thus more simplified architecture, and varying Young's moduli for teeth are compared against an original model with more accurate internal and external architecture. To investigate the effects of these simplifications, the performance of each macaque model, built using a specific modeling approach, is compared with each other model for simulated first incisor (I^1), first premolar (P^1), and second molar (M^2) unilateral bites. The findings in the macaque are also compared to those from a different species, *Cercocebus atys*, under a simulated I^1 bite to assess the magnitudes of errors in relation to the differences between species. We use two approaches to compare performance: strain magnitudes and contour maps to assess local deformations, and geometric morphometric analyses of size and shape to assess large scale deformations. How the differences between bites and species compare to those among modeling simplifications is relevant to understanding the impact of modeling simplifications.

MATERIALS AND METHODS

The cranium of an adult male *Macaca fascicularis* (our catalogue number Mac17) and an adult male *Cercocebus atys* (referred to as C13.21) were segmented from microCT scans (voxel size: Mac17; 0.142 × 0.142 × 0.142 mm and C13.21; 0.122 × 0.122 × 0.244, X-Tek HMX 160 μCT system; X-Tek Systems, Tring, UK) using Avizo image processing software (Visualisation Sciences Group, USA) with bone and teeth as separate materials. A combination of thresholding and manual segmentation was applied to create models with a high degree of anatomical accuracy representing a minimal amount of simplification. Both models were subsequently downsampled to the same voxel size (0.428 × 0.428 × 0.428 mm). These are referred to as model 1. A series of new models was then constructed for the macaque by progressively filling in spaces within the internal bone. The second macaque model (model 2) therefore consisted of the original macaque model 1 with all the foramina, air cells (i.e., mastoid air cells) and trabecular bone filled with cortical bone. The third model (model 3) consisted of model 2 with the maxillary sinuses also filled, we refer to this as the 'solid' model. All models were converted into finite element (FE) meshes consisting of between 724,095 and 997,175 eight-noded cubic elements using custom software. These were imported into VOX-FE, our custom FEA pre- and postprocessing voxel based software (Liu et al., 2011). All materials were modeled as linear elastic and isotropic with a Poisson's ratio of 0.3. Bone was assigned a Young's modulus of 17 GPa (Kupczik et al., 2007) and teeth, 70 GPa (tooth enamel; Kupczik et al., 2007, Strait et al., 2009). In a further test of model simplification, the teeth in the macaque models were subsequently given the material properties of bone and all models re-run. We designate macaque models, with teeth assigned material properties close to that of enamel (70 GPa) as models 1a–3a, and those with teeth allocated the material properties of bone (17 GPa) as models 1b–3b.

To accurately load the specimen, muscle attachments and physiological cross-sectional areas (PCSAs) that were previously ascertained via dissection (Kupczik et al., 2007) were used for the macaque model. PCSAs for all muscles were calculated following the protocol of Anapol and Barry (1996). Unfortunately the superior head of the lateral pterygoid was not dissected on this individual. Instead we used PCSA data published in

Antón (2000) for the upper range of *M. fascicularis* females. Peak muscle forces (F_{max}) were calculated by multiplying the PCSA of each muscle by a muscle stress constant of 37 N/cm^2 (Weijs and Hillen, 1985). PCSA data are not available for the *Cercocebus* specimen. As such, muscle cross-sectional areas were estimated from bony proxies. These included the myogonial angle area for the medial pterygoid, and the area between the zygo-
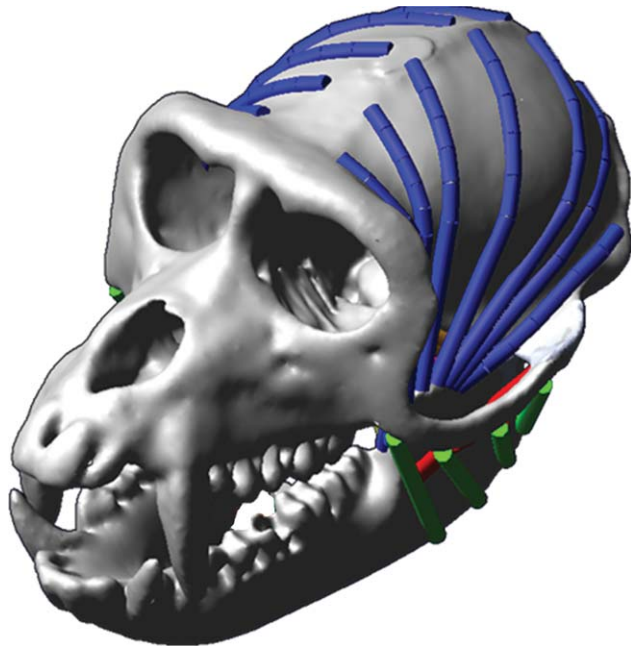

Fig. 2. Multibody dynamic analysis (MDA) model of *Macaca fascicularis* using an optimization criterion that minimizes the sum of squared muscle stresses. Muscle activation patterns are predicted for bites at each tooth with the jaw rotated by three degrees and for a biting force of 100 N and maximum predicted biting force. The mandible and cranium are treated as rigid bodies with contact points at the left and right temporomandibular joints. Muscles are modeled as a series of strands: green = superficial masseter; red = deep masseter; blue = anterior and posterior aspect of temporalis muscle. The medial pterygoid and lateral pterygoid are not visible.

matic arch and the ramus for the masseter (see Antón, 1999, 2000) and the infratemporal fossa for the temporalis (Demes and Creel, 1988). These values were then scaled by a correction factor (calculated as: actual Mac17 PCSA/Mac17 cross-sectional area predicted via bony proxies).

The muscle forces required to produce maximal force during a particular bite were predicted via multibody dynamic analysis (MDA) (Fig. 2), an engineering technique which allows for the simulation of jaw motion and forces (Curtis et al., 2008, 2010; Fitton et al., 2012; Shi et al., 2012). The muscle force generated in any particular biting task is the product of F_{max}, the muscle's active force/length relationship, the muscle's stress (N/cm^2), activation factor, and passive muscle tension. In our modeling, the passive tension of the muscle reached a maximum of 0.3 N (Curtis et al., 2009). Thus, the force produced by each muscle group in each particular bite was principally controlled by the unknown activation factor. The activation factor was specified as a design variable within a specialist unit of ADAMS (ADAMS/Insight, MSC Software, USA), and defined to have a range of zero to one (i.e., no activity to 100% activity). Muscle activations were estimated using minimization of total muscle energy (proportional to muscle stress) as the optimization criterion for various biting tasks (Rasmussen et al., 2001; Heintz and Gutierrez-Farewik, 2007; Fitton et al., 2012; Shi et al., 2012) whilst maintaining a stable temporomandibular joint (TMJ). MDA estimated maximal biting forces (Shi et al., 2012) during I^1, P^1, and M^2 bites along the dental row at three degrees of jaw opening, as well as the optimal muscle activation pattern, and thus muscle forces in Newtons (N), for the individual biting task for both *Macaca* and *Cercocebus* (Table 1). Interestingly, the MDA solution results in maximal anterior temporalis muscle activation in all three bites, on both the working and balancing sides. This is not surprising given the criterion of maximal biting force, the line of action of this muscle and its lever mechanics. Stability of the TMJ during maximal biting was achieved by submaximal and varied activations of the remaining muscle components. These predicted muscle forces were applied to each macaque model in the same way to ensure that any differences in performance were due to simplification approach rather

TABLE 1. Maximum muscle forces predicted for *Macaca fascicularis* (Mac17) and *Cercocebus atys* (C13_21) via multibody dynamic analysis (MDA) for the working (W) and balancing (B) side

	Muscle force (N)							
	Macaca fascicularis						*Cercocebus atys*	
	W			B			I^1	
Muscle	I^1	P^1	M^2	I^1	P^1	M^2	W	B
Anterior temporalis	124.4	124.4	124.4	124.4	124.4	124.4	132.4	175.9
Posterior temporalis	51.7	83.9	85.9	97.8	121.6	124.4	48.6	10.5
Deep masseter	37.7	49.2	49.5	58.5	46.9	45.8	72.7	16.2
Superficial masseter	82.3	96.0	95.5	90.4	85.7	85.9	102.4	62.7
Medial pterygoid	97.2	101.3	103.0	93.1	95.2	98.1	24.2	131.1
Sup. lat. pterygoid[a]	1.3	0.1	0.4	1.1	0.4	0.0	2.9	0.3

Note the MDA solution results in maximal anterior temporalis muscle activation in all three bites, on both the working and balancing sides and is not surprising given the criterion of maximal biting force, the line of action of this muscle and its lever mechanics.

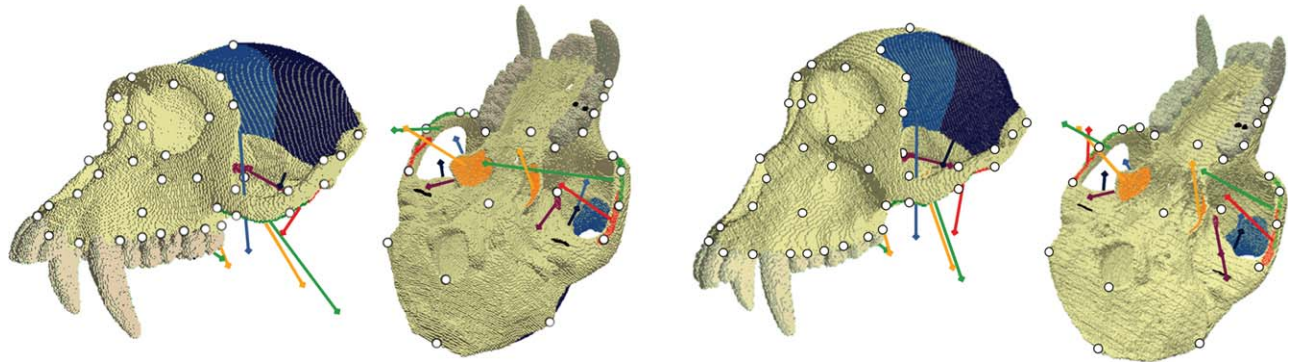[a]Sup. lat. pterygoid; the superior head of the lateral pterygoid.

Fig. 3. Finite element (FE) model boundary conditions for *Macaca fascicularis* (left) and *Cercocebus atys* (right). Muscle forces represent the major muscles of mastication: green = superficial masseter; red = deep masseter; orange = medial pterygoid; purple = superior lateral pterygoid; dark blue = posterior temporalis; and light blue = anterior temporalis. The glenoid fossae are constrained in all directions and the bite points are constrained in the vertical axis. An M2 bite is illustrated (black points are the constraints). The 70 sampling points are shown on both specimens. Strain magnitudes and three-dimensional coordinates are extracted at these points for comparisons of local and large scale deformations.

than applied muscle forces. Bites were simulated on the left I^1, P^1, and M^2. The FE models (Fig. 3) were all constrained at the working side tooth in the infero-superior direction and the glenoid fossae in all three directions (*x, y, z*). The original *Cercocebus* MDA and FEA models with teeth modeled as bone (model 1a) were solved for an I^1 bite only.

The finite element analyses predicted cranial deformations for each model and load case. Here we use the term 'deformation' to refer to local and global changes in the size and shape of an object but not rigid body motions. The FE predictions of cranial deformation due to simulated biting were proportionately scaled to represent the deformations that would result from a bite force of 100 N on each tooth. This is straightforward since deformation increases linearly and proportionately with load magnitude (Hooke's law; see Milne and O'Higgins, 2013; O'Higgins and Milne, 2013) facilitating comparisons of error magnitudes (which scale similarly with bite force) between bites.

Von Mises strain contour maps showing the simulated, scaled cranial responses to loading were compared in terms of the distributions and magnitudes of strains. Additionally, maximum and minimum principal strains were recorded from the *Macaca* and *Cercocebus* models at 70 sampling points chosen for comparability with a previous sensitivity study of the effects of varying muscle activations (Table 2; Fitton et al., 2012).

Large scale deformations were also compared between models using geometric morphometric methods applied to the coordinates of the 70 landmarks listed in Table 1. A sensitivity analysis in Fitton et al. (2012), showed that reducing the number of landmarks from 300 landmarks and semilandmarks to 70 landmarks had little effect on the resulting assessment of large scale deformations. Given that semilandmarks cannot be reliably located in equivalent locations on different crania, this study confines itself to the 70 landmarks alone.

In this study, large scale deformations of the crania were compared among load cases and between models by submitting the coordinates of the 70 landmarks (Table 2), before and after loading, to a Procrustes size and shape analysis (O'Higgins and Milne, 2013). When comparing deformations arising from FEA, it is neces-

TABLE 2. 70 cranial landmarks and their anatomical definitions

Number[a]	Landmark definition[b]
1	Centre point between incisors at alveolar margin
2	Premaxillary suture at inferior margin of nasal aperture
3	Tip of nasal bones in midline
4	Nasofrontal suture in the midline
5	Upper margin of supraorbital rim in the midline
6	Bregma
7	External occipital protuberance
8	Basilar
9	Midline of transverse palatine suture
10&38	Uppermost centre point on orbital aperture
11&39	Most lateral part of nasal aperture
12&40	Inferior border of alveolar margin between I^2 and C
13&41	Inferior border of alveolar margin between C and P^1
14&42	Inferior border of alveolar margin between P^1 and P^2
15&43	Inferior border of alveolar margin between P^2 and M^1
16&44	Inferior border of alveolar margin between M^1 and M^2
17&45	Inferior border of alveolar margin between M^2 and M^3
18&46	Inferior border of alveolar margin behind M^3
19&47	Superior apex of the inferior orbital fissure
20&48	Porion
21&49	ZM suture on the inferior orbital margin
22&50	ZF suture on the lateral orbital margin
23&51	Frontolacrimal suture on the medial orbital margin

[a]The number on the left corresponds to the anatomical left, the subsequent number is the anatomical right (Left & Right)
[b]ZM; zygomaticomaxillary suture, ZT; zygomaticotemporal suture, ZF zygomaticofrontal suture.
These landmarks are used in both the comparison of bone strain magnitude between models (Tables 3 and 4) and the GM analyses (Figs. 6 and 7).

sary for differences in both size and shape to be accounted. This is because an object under loading will deform, and the subsequent displacements of landmarks will reflect changes in both size and shape. In earlier, similar studies combining GM methods and FEA results, Procrustes form analysis (called size-shape space in Mitteroecker et al., 2004) was used (shape variables plus the log of centroid size; Cox et al., 2011; Gröning et al., 2011; Fitton et al., 2012). However, as discussed by O'Higgins and Milne (2013), logging of centroid size rescales this component relative to shape in such a way that a relatively lower weighting is given to the size differences. This is not desirable since the changes in size under loading are of equal significance in mechanical terms as changes in shape. As such, the present study uses Procrustes "size and shape" analysis (Dryden and Mardia, 1999; Dryden et al., 2007; O'Higgins and Milne, 2013).

The size and shape analysis comprises the translation and rotation (but not scaling) steps of generalized Procrustes analysis (GPA), minimizing the least squares distances between unscaled configurations (Kendall et al., 1999; Dryden et al., 2007). Since the deformations resulting from FEA are very small, the impact that variations in size might have on, for example, the estimation of means (O'Higgins and Milne, 2013) is minimal. By omitting the scaling step, the resulting distances, between loaded and unloaded models, are the consequence of differences in both size and shape.

Thus, in our first GM analysis of *Macaca* alone, after scaling displacements of landmarks according to bite force, the coordinates of the unloaded and loaded models are translated and rotated but not scaled to minimize the size and shape distances among specimens. The resulting size and shape variables from the six different macaque models (1a–3a and 1b–3b) loaded in three different ways (I^1, P^1, and M^2 bites) and the unloaded model were then submitted to PCA. In the second GM analysis, the landmark coordinates of these models and load cases were combined with those from the *Cercocebus atys* model (unloaded and I^1 biting simulation). The size and shape differences between specimens were very large compared to the differences that arise when a model is loaded. Thus, to focus the analysis on the latter scenario, the differences in size and shape between the unloaded models of both species were discounted. This was achieved as follows: first, the displacements between landmark coordinates for the unloaded and loaded models were computed. These were then scaled, as above, according to bite force and added to the respective original unloaded *M. fascicularis* or *C. atys* landmark configurations. These coordinates were then subjected to GPA and the differences in coordinates (residuals) between each loaded and unloaded model extracted. The mean unloaded model shape was calculated and the residuals were added to it. The centroid size of each load case was then multiplied by the ratio of loaded/unloaded centroid size for each model. The resulting scaled centroid sizes were then applied to the [mean + residual] landmark configurations of each loaded model. This restores differences in such a way that relative changes in scale, as a consequence of loading, are preserved. These data were then subjected to a size and shape analysis as above. This approach leads to a quantification and visual assessment of differences in (global, large scale) deformation due to the different modeling approximations and load cases in both species.

The macaque surface was used in both analyses to visualize the aspects of differences in size and shape represented in the resulting PC plots. In the analysis combining both species, the macaque surface was first warped to the mean landmark configuration of the unloaded models, creating a mean macaque–cercocebus surface. The results are presented as principal component plots and visualized using warpings of the surface together with superimposed transformation grids (calculated using thin plate splines; Bookstein, 1989). To aid interpretation the deformations of these are magnified 500 times. The resulting transformation grids do not adequately represent the true deformation of material due to loading; rather, they are a visual device to aid interpretation (Weber et al., 2011; O'Higgins and Milne, 2013). The Geometric Morphometric analyses were carried out using the EVAN toolbox (http://www.evan-society.org).

RESULTS
Differences Between Bites

The strain contour maps of the *Macaca fascicularis* models under I^1, P^1, and M^2 100N bite loading scenarios (Figs. 4 and 5) differ. During incisor bites in all *M. fascicularis* models, regardless of segmentation simplification (models 1ab-3ab), elevated strain magnitudes are present at the premaxillary region and along the nasal margin. These regions are less strained during premolar bites, instead the mid facial and maxillary regions superior to the premolars present higher levels of strain than observed during incisor or molar bites. During M^2 bites, strain in these regions reduces and a slight elevation in strain is observed over the maxillary root of the zygomatic arch. During all three load cases, strain over the zygoma and zygomatic arch is high (Fig. 4).

Tables 3 and 4 present values for maximum ($\epsilon 1$) and minimum ($\epsilon 3$) principal strains that complement the contour plots of von Mises strain (Figs. 4 and 5). Regardless of model build the greatest predicted strains occur during incisor bites at the superior root of the zygomatic arch (landmark 54, $\epsilon 1$; between 658 με and 677 με, depending on model) and at the zygomaticomaxillary suture at the inferior root of the zygomatic arch (landmark 53 and 25, $\epsilon 3$; between −794 and −768 με) (Tables (3 and 4)). Strains at these points remain the greatest overall in each biting simulation but decrease with more posterior bites: premolar bites ($\epsilon 1$; between 395 and 402 με, $\epsilon 3$; between −507 and −513 με) and molar bites ($\epsilon 1$; between 270 and 277 με, $\epsilon 3$; between −345 and −392 με) (Tables 3 and 4). The average predicted strains in the macaque models at the 70 landmarks during incisor bites range between 102 and 116 με ($\epsilon 1$) and −107 to −122 με ($\epsilon 3$). During premolar bites, the average strain is between 63 and 68 με ($\epsilon 1$) and −68 to −73 με ($\epsilon 3$), decreasing during molar bites to 41–47 με ($\epsilon 1$) and −43 to −52 με ($\epsilon 3$) (Tables 3 and 4). At a single landmark, the maximum difference in recorded strain between bites is 402 με. This occurs between the incisor and molar bites and is recorded at the superior root of the zygomatic arch (landmark 54, model 1b, Table 4).

Effect of Filling Small Cavities and Trabecular Bone

Strain contour maps show small differences as models are increasingly filled (models 1–2; Figs. 4 and 5). These

Teeth modelled with a Young's modulus of 70GPa

Fig. 4. Von Mises strain predicted for three different load cases (I^1, P^1, and M^2, 100 N bite force) for differently segmented models with teeth modeled with dental material properties. Model 1a: original *Macaca fascicularis* model segmented with anatomical accuracy; model 2a: simplified such that all the foramina, air cells (i.e., mastoid air cells) and cancellous bone cavities are filled with material indistinguishable from cortical bone; model 3a: a variant of model 2a with the maxillary sinuses also filled with cortical bone.

are most pronounced between models 1a and 1b and models 2a and 2b during premolar and molar bites and where strains are found over the maxilla above the premolars and over the zygoma (Figs. 4 and 5). The point measurements of maximum and minimum principal strains (Tables 3 and 4) in models 1 and 2 also show a decrease directly above the premolars (landmark 67). At this location $\epsilon 1$ values decrease by around 20 $\mu\epsilon$ during premolar bites as the models are increasingly filled (decreasing from 80 to 58 $\mu\epsilon$ comparing models 1a and 2a; and 91–67 $\mu\epsilon$, comparing models 1b and 2b; Tables 3 and 4). Average strains over all 70 cranial landmarks decrease by only 2–6 $\mu\epsilon$ regardless of bite (Tables 3 and 4). At the majority of sampling points (73–96%) during

I^1, P^1, and M^2 bites, changes are less than 10 $\mu\epsilon$. However, several areas experience more significant changes in strain. Notably, when comparing models 1 and 2, the region above the working side porion (landmark 48), shows a substantial reduction in $\epsilon 3$ of 56 $\mu\epsilon$ (during I^1) and 28 $\mu\epsilon$ (during M^2) (Table 3).

Effect of Filling the Maxillary Sinus

Strain contour maps show minimal differences over the surface following filling of the maxillary sinuses. Comparing models 2a and 2b (cancellous bone and small cavities filled) with models 3a and 3b (model 2 plus filled maxillary sinus; Figs. 4 and 5), small differences are

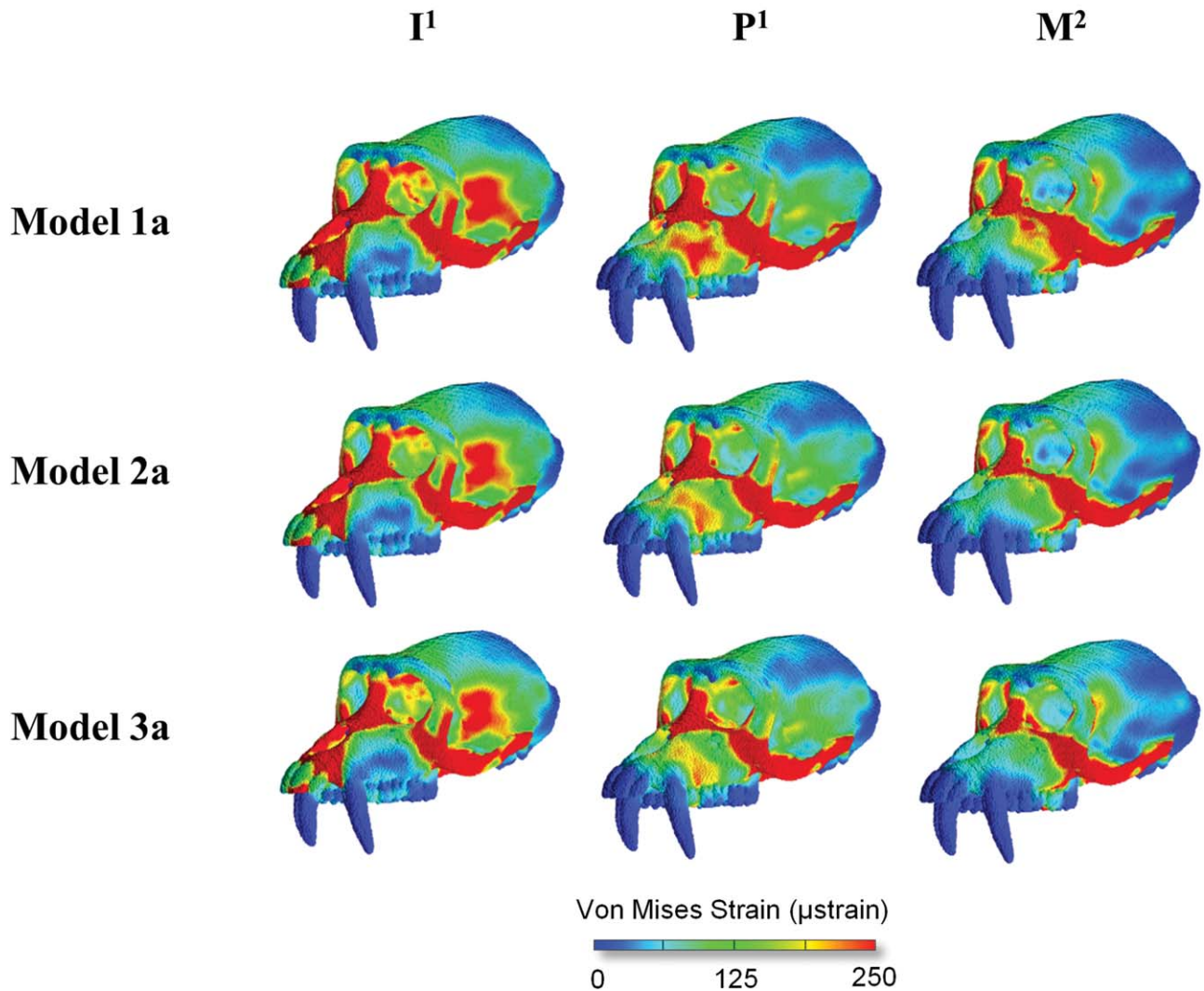# Teeth modelled with a Young's modulus of 17GPa
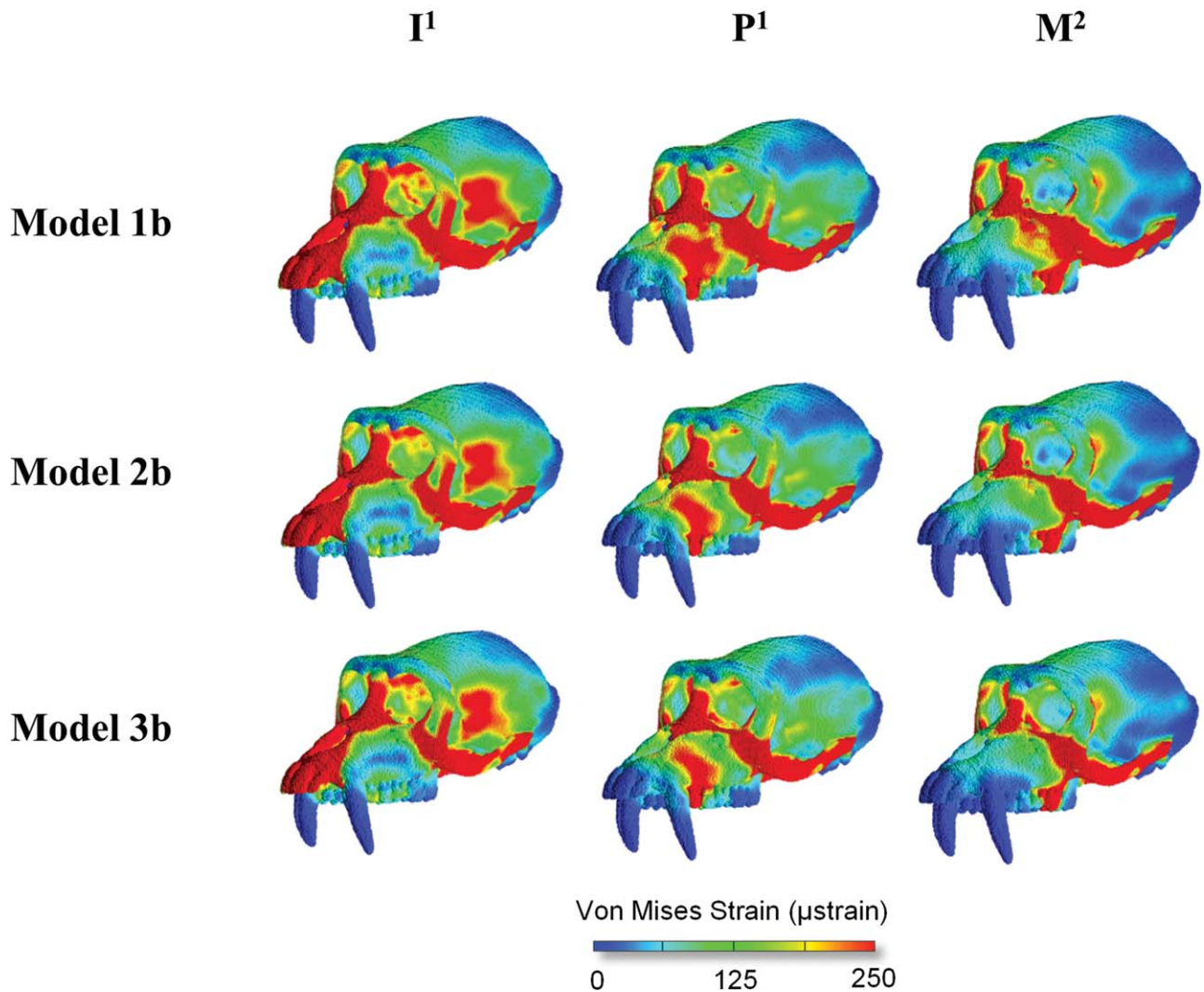
Fig. 5. Von Mises strains predicted for three different load cases (I^1, P^1, and M^2 100 N bite force) for differently segmented models with teeth modeled with cortical bone material properties. Model 1b: original *Macaca fascicularis* model segmented with anatomical accuracy; model 2b: simplified such that all the foramina, air cells (i.e., mastoid air cells) and cancellous bone cavities are filled with material indistinguishable from cortical bone; model 3b: a variant of model 2b with the maxillary sinuses also filled with cortical bone.

evident. Values for maximum and minimum principal strains (Tables 3 and 4) highlight the observations from the contour plots; average strains over the 70 cranial landmarks decrease by 2–8 με regardless of bite point (Tables 3 and 4), with the majority of landmarks (89–96%) experiencing only small changes in strain, of less than 10 με during I^1, P^1, and M^2 bites. Differences of only a few με are recorded between models 2–3 at surface landmarks overlying the maxillary sinus (landmarks 66 and 69) and the maxillary region above the premolars (landmark 67 and 70; Tables 3 and 4). Several areas record a change in strain greater than 10 με; these include the premaxillary suture at the inferior margin of

the nasal aperture. At this point, there is a reduction in ε1 by 15–38 με (landmark 2; Tables 3 and 4).

Effects of Varying Dental Material Properties

Von Mises strain contour maps differ between models a and b, mainly in showing lower strain magnitudes over the alveolus local to the loaded tooth when it is modeled with the material properties of bone (17 GPa; Fig. 5) rather than enamel (70 GPa; Fig. 4). Maximum and minimum principal strains show the greatest differences between models 1a (enamel material properties) and 1b (bone properties) during incisor bites (Tables 3

TABLE 3. Maximum (ϵ1) and minimum principal strains (ϵ3) recorded at 70 cranial locations during a 100 N incisor bite (I^1), premolar bite (P^1), and molar bite (M^2), models 1a–3a

Landmark	Maximum Principal Strain									Minimum Principal Strain								
	Incisor			Premolar			Molar			Incisor			Premolar			Molar		
Model	1a	2a	3a	1a	2a	3a	1a	2a	3a	1a	2a	3a	1a	2a	3a	1a	2a	3a
1	21	21	20	4	3	2	3	3	2	−22	−22	−22	−2	−1	−1	−2	−2	−1
2	253	237	205	61	57	40	46	41	29	−67	−62	−54	−21	−20	−14	−17	−15	−11
3	87	83	71	33	32	27	16	16	13	−46	−43	−38	−18	−17	−15	−8	−8	−6
4	71	68	64	44	42	39	23	22	20	−231	−219	−205	−134	−127	−118	−62	−59	−52
5	3	3	3	10	9	9	12	11	10	−2	−3	−3	−7	−7	−6	−7	−7	−6
6	19	19	19	14	14	14	9	9	9	−33	−33	−33	−24	−24	−24	−16	−16	−16
7	5	5	5	6	5	5	6	5	5	−2	−1	−1	−2	−2	−2	−2	−1	−1
8	47	23	24	27	14	14	18	12	12	−17	−13	−13	−11	−7	−7	−16	−10	−9
9	37	23	52	31	29	43	12	14	21	−14	−10	−20	−13	−16	−20	−8	−11	−12
10	66	68	62	78	74	69	63	58	55	−29	−29	−27	−32	−30	−29	−25	−23	−22
11	77	77	77	105	104	96	48	45	37	−234	−232	−236	−30	−30	−27	−15	−13	−11
12	278	278	279	13	13	11	9	8	6	−103	−101	−99	−43	−42	−38	−18	−20	−17
13	59	51	48	81	76	74	8	7	4	−13	−13	−13	−66	−45	−43	−6	−3	−2
14	6	7	8	32	32	33	3	2	1	−8	−8	−8	−23	−25	−25	−7	−4	−3
15	61	80	86	32	28	36	35	26	19	−21	−26	−28	−12	−12	−16	−36	−32	−26
16	42	37	38	21	16	17	18	16	19	−16	−13	−12	−77	−63	−54	−74	−57	−54
17	16	18	14	12	12	9	8	8	5	−60	−66	−50	−44	−45	−32	−26	−29	−16
18	20	13	18	11	11	7	25	16	5	−25	−18	−20	−12	−11	−9	−38	−21	−7
19	15	16	16	22	19	17	24	19	15	−13	−16	−15	−13	−11	−10	−14	−10	−7
20	58	35	35	34	20	20	14	8	8	−125	−87	−87	−81	−55	−55	−34	−22	−23
21	146	137	123	163	133	119	121	94	81	−47	−43	−38	−50	−41	−36	−37	−29	−24
22	26	22	20	25	25	22	29	27	25	−37	−37	−32	−70	−69	−62	−80	−74	−67
23	87	83	76	70	68	63	41	40	38	−310	−294	−270	−254	−245	−228	−146	−142	−134
24	100	94	88	67	65	62	23	23	21	−320	−303	−282	−214	−209	−198	−75	−74	−69
25	190	190	194	186	185	187	143	143	144	−515	−513	−525	−513	−507	−511	−390	−389	−392
26	347	350	356	330	330	334	248	248	251	−126	−125	−125	−110	−109	−110	−79	−79	−80
27	121	120	121	105	104	105	75	75	75	−196	−193	−195	−171	−170	−170	−124	−123	−123
28	50	50	45	56	38	28	73	53	37	−73	−52	−51	−31	−11	−10	−28	−12	−10
29	15	14	14	8	7	6	14	13	9	−40	−37	−37	−9	−8	−9	−6	−5	−4
30	97	99	87	84	82	73	61	56	50	−30	−30	−27	−26	−25	−22	−19	−17	−15
31	44	42	39	3	3	3	6	6	6	−16	−15	−15	−3	−3	−3	−15	−13	−12
32	111	109	109	96	95	95	66	66	66	−262	−259	−258	−226	−224	−224	−156	−156	−156
33	160	160	156	99	100	98	54	55	53	−58	−58	−57	−43	−43	−42	−28	−28	−27
34	3	2	2	1	1	1	0	0	0	−4	−3	−3	−2	−1	−1	−1	0	0
35	88	88	87	71	71	70	47	47	46	−85	−85	−84	−67	−67	−67	−45	−45	−45
36	272	273	272	226	228	227	152	153	152	−282	−286	−284	−225	−229	−228	−149	−151	−150
37	5	1	2	7	4	4	7	6	6	−1	−1	−2	−2	−1	−1	−2	−2	−2
38	35	38	33	8	8	7	6	6	6	−14	−15	−13	−17	−15	−17	−17	−17	−20
39	56	56	58	12	12	13	3	4	4	−201	−204	−210	−43	−45	−45	−12	−14	−14
40	362	360	361	66	65	62	19	22	20	−102	−99	−98	−17	−17	−16	−6	−6	−5
41	21	19	17	3	3	3	1	1	1	−15	−12	−13	−7	−4	−4	−3	−1	−1
42	30	45	51	2	5	9	1	1	3	−29	−28	−29	−12	−7	−7	−6	−2	−2
43	20	31	41	3	4	8	1	1	1	−22	−20	−22	−9	−6	−5	−7	−3	−1
44	7	4	2	5	3	1	3	2	1	−22	−16	−8	−12	−9	−5	−7	−6	−3
45	25	20	12	16	13	8	10	8	5	−30	−21	−8	−21	−18	−8	−14	−12	−7
46	19	18	13	18	14	11	12	9	7	−68	−41	−40	−24	−16	−15	−10	−8	−7
47	8	16	11	9	9	10	9	9	11	−17	−18	−13	−16	−13	−16	−14	−12	−16
48	70	46	47	51	36	36	33	24	24	−197	−141	−141	−148	−107	−106	−99	−71	−71
49	205	198	168	78	78	66	46	43	36	−71	−66	−57	−28	−26	−23	−17	−15	−13
50	75	65	61	80	74	73	64	61	62	−56	−53	−46	−36	−34	−31	−26	−25	−24
51	88	84	75	21	20	17	17	14	17	−249	−237	−210	−64	−58	−47	−17	−14	−10
52	95	89	82	29	29	25	14	14	12	−350	−327	−301	−82	−78	−69	−39	−39	−35
53	265	269	273	160	162	164	110	111	112	−775	−784	−794	−469	−474	−479	−322	−324	−327
54	664	666	677	397	397	402	275	273	277	−219	−218	−221	−132	−131	−132	−91	−90	−91
55	279	271	268	172	168	166	115	112	111	−527	−517	−518	−319	−313	−313	−217	−213	−213
56	49	49	41	14	19	15	9	10	7	−75	−51	−62	−15	−13	−21	−9	−6	−10
57	18	17	17	16	15	16	12	12	12	−48	−46	−46	−43	−41	−42	−33	−32	−33
58	28	30	25	7	7	5	3	3	2	−17	−17	−15	−5	−5	−4	−3	−3	−3
59	59	55	52	60	57	57	48	47	47	−20	−18	−18	−19	−18	−18	−15	−15	−15
60	95	95	94	56	55	55	38	37	37	−310	−308	−306	−182	−179	−178	−124	−122	−120
61	161	157	152	104	103	100	69	69	68	−63	−63	−62	−39	−39	−38	−26	−26	−26
62	4	3	3	3	2	2	2	1	1	−7	−8	−8	−5	−5	−5	−2	−2	−2
63	166	164	161	97	96	94	65	64	63	−78	−77	−76	−44	−44	−44	−30	−29	−29
64	470	471	470	269	269	268	182	182	182	−433	−430	−425	−265	−263	−260	−180	−179	−178
65	185	190	169	122	120	102	57	56	48	−170	−146	−137	−101	−84	−81	−33	−26	−24
66	206	208	211	184	183	185	129	129	131	−78	−80	−82	−91	−95	−95	−69	−74	−75
67	6	3	4	80	58	52	23	18	14	−8	−5	−5	−85	−71	−67	−22	−13	−10
68	185	193	188	70	73	68	36	37	33	−156	−130	−133	−51	−41	−41	−22	−18	−18
69	352	331	336	203	191	195	134	126	129	−97	−82	−83	−51	−41	−40	−33	−26	−25
70	35	25	32	11	10	13	6	4	4	−36	−14	−22	−10	−4	−7	−3	−1	−2
min	3	1	2	1	1	1	0	0	0	−1	−1	−1	−2	−1	−1	−1	0	0
max	664	666	677	397	397	402	275	273	277	−774.7	−784.5	−794	−512.5	−507.2	−510.8	−389.9	−389.3	−392.3
average	106	104	102	67	64	63	45	42	41	−115	−109	−107	−73	−69	−68	−48	−45	−43

Teeth modeled with dental material properties (70 GPa). Values are in microstrain ($\mu\epsilon$).

TABLE 4. Maximum (ε1) and minimum principal strains (ε3) recorded at 70 cranial locations during a 100 N incisor bite (I^1), premolar bite (P^1), and molar bite (M^2), models 1b–3b

Landmark	Maximum Principal Strain									Minimum Principal Strain								
	Incisor			Premolar			Molar			Incisor			Premolar			Molar		
Model	1b	2b	3b	1b	2b	3b	1b	2b	3b	1b	2b	3b	1b	2b	3b	1b	2b	3b
1	119	118	117	12	11	8	8	8	6	−128	−128	−127	−4	−3	−3	−3	−2	−2
2	352	329	291	62	58	37	42	40	25	−91	−89	−87	−21	−19	−12	−14	−13	−8
3	95	90	78	33	32	27	23	22	18	−50	−47	−41	−18	−17	−15	−12	−12	−10
4	72	68	65	45	43	39	31	29	27	−234	−222	−209	−136	−129	−120	−93	−88	−82
5	3	3	2	11	10	9	7	7	6	−2	−3	−3	−7	−8	−7	−5	−5	−5
6	19	19	19	14	14	14	10	9	10	−34	−33	−33	−24	−24	−25	−17	−17	−17
7	5	5	5	6	5	5	4	3	3	−2	−1	−1	−2	−2	−2	−1	−1	−1
8	47	23	24	27	14	14	19	10	10	−17	−13	−13	−11	−7	−7	−8	−4	−5
9	48	33	63	36	33	48	24	22	33	−17	−13	−23	−14	−16	−20	−10	−11	−14
10	65	66	61	79	75	70	54	51	48	−33	−29	−27	−33	−31	−29	−22	−21	−20
11	106	105	106	109	107	99	75	73	68	−334	−332	−335	−31	−30	−28	−21	−21	−19
12	264	264	263	7	7	7	5	5	4	−82	−81	−80	−26	−26	−23	−18	−17	−16
13	126	90	87	85	73	71	58	50	49	−30	−24	−24	−182	−148	−146	−124	−102	−100
14	17	18	18	51	52	52	35	35	36	−20	−20	−20	−63	−67	−67	−43	−46	−46
15	155	170	168	26	35	45	18	24	31	−47	−50	−50	−17	−16	−20	−11	−11	−14
16	45	37	42	21	16	18	14	11	12	−13	−12	−14	−63	−52	−43	−43	−36	−29
17	17	17	15	13	13	7	9	9	5	−60	−64	−44	−46	−46	−29	−32	−32	−20
18	25	19	24	11	11	11	8	7	8	−29	−25	−24	−15	−13	−13	−10	−9	−9
19	15	15	15	22	19	17	15	13	12	−14	−16	−15	−13	−11	−10	−9	−8	−7
20	59	35	35	34	19	20	23	13	14	−125	−87	−87	−80	−54	−55	−55	−37	−37
21	143	136	122	169	137	123	116	94	84	−46	−43	−38	−52	−42	−37	−36	−29	−25
22	30	25	23	25	25	22	17	17	15	−38	−37	−32	−71	−69	−63	−48	−47	−43
23	88	84	78	73	70	65	50	48	44	−315	−299	−277	−263	−253	−235	−180	−173	−161
24	109	103	97	71	70	67	49	48	46	−347	−328	−310	−227	−224	−213	−156	−153	−146
25	187	187	192	185	184	186	126	126	127	−505	−505	−519	−509	−504	−509	−348	−345	−348
26	343	346	354	328	328	333	224	225	228	−126	−125	−125	−110	−109	−110	−75	−75	−75
27	120	120	121	104	104	104	71	71	71	−195	−193	−194	−171	−169	−170	−117	−116	−117
28	62	59	53	58	39	29	40	26	20	−93	−71	−67	−36	−14	−14	−24	−9	−10
29	16	15	15	8	7	6	5	5	4	−43	−39	−39	−10	−8	−9	−7	−6	−6
30	98	100	87	87	84	75	59	58	51	−30	−30	−27	−27	−26	−23	−18	−18	−16
31	48	45	42	3	3	4	2	2	2	−18	−16	−16	−3	−3	−3	−2	−2	−2
32	111	109	109	96	95	95	65	65	65	−262	−258	−258	−226	−224	−224	−155	−153	−153
33	163	163	158	100	101	99	69	69	68	−59	−59	−58	−43	−43	−42	−29	−29	−29
34	3	2	2	1	1	1	1	0	0	−4	−3	−3	−2	−1	−1	−1	−1	−1
35	88	88	87	71	71	70	48	49	48	−85	−85	−84	−67	−67	−67	−46	−46	−46
36	273	274	273	227	228	227	155	156	155	−283	−288	−285	−226	−229	−228	−154	−157	−156
37	6	1	1	7	5	4	5	3	3	−2	0	−2	−2	−1	−1	−2	−1	−1
38	33	36	32	8	8	7	5	5	5	−14	−14	−13	−19	−17	−19	−13	−12	−13
39	71	72	74	13	14	14	9	9	10	−256	−261	−269	−47	−50	−50	−32	−34	−34
40	337	333	333	55	54	51	38	37	35	−83	−82	−81	−13	−13	−12	−9	−9	−9
41	72	61	55	13	12	10	9	8	7	−22	−20	−21	−7	−5	−5	−5	−3	−3
42	94	94	92	15	18	18	10	12	12	−53	−47	−48	−15	−11	−10	−10	−8	−7
43	73	82	92	10	13	19	7	9	13	−47	−40	−39	−13	−10	−8	−9	−7	−6
44	12	6	4	9	6	2	6	4	1	−35	−26	−9	−22	−19	−5	−15	−13	−4
45	24	21	15	15	13	7	10	9	5	−23	−19	−8	−18	−16	−7	−12	−11	−4
46	13	13	9	14	11	9	9	7	6	−62	−39	−37	−20	−15	−14	−14	−10	−10
47	10	18	11	9	9	11	6	6	7	−19	−20	−15	−16	−14	−17	−11	−9	−12
48	71	46	46	51	36	36	35	25	25	−197	−141	−141	−149	−107	−107	−102	−73	−73
49	205	200	169	74	75	62	51	51	43	−72	−67	−58	−26	−25	−22	−18	−17	−15
50	80	70	66	85	78	77	58	53	52	−57	−54	−47	−38	−35	−32	−26	−24	−22
51	90	86	78	20	19	16	13	13	11	−254	−244	−217	−59	−55	−45	−41	−37	−31
52	103	96	89	30	30	25	20	20	17	−370	−344	−322	−76	−72	−64	−52	−49	−44
53	262	267	272	159	161	163	109	110	112	−768	−780	−791	−466	−472	−477	−319	−323	−327
54	658	661	673	395	395	401	270	270	274	−217	−217	−220	−131	−130	−132	−90	−89	−90
55	280	272	269	172	168	166	118	115	114	−526	−516	−518	−319	−313	−313	−218	−214	−214
56	58	57	49	14	20	15	10	13	11	−103	−77	−87	−17	−16	−25	−11	−11	−17
57	19	18	18	16	16	16	11	11	11	−50	−48	−49	−44	−43	−44	−30	−29	−30
58	29	30	25	6	7	5	4	4	3	−17	−17	−15	−5	−5	−4	−3	−3	−3
59	63	58	55	63	60	59	43	41	40	−21	−19	−18	−20	−19	−19	−14	−13	−13
60	95	94	94	56	55	55	38	38	37	−310	−308	−306	−182	−179	−178	−124	−122	−122
61	164	159	154	105	104	101	72	71	69	−64	−63	−62	−39	−39	−38	−27	−27	−26
62	4	3	3	3	2	2	2	1	1	−7	−8	−8	−5	−5	−5	−3	−3	−3
63	167	165	162	98	96	95	67	66	65	−78	−77	−77	−44	−44	−44	−30	−30	−30
64	471	472	470	269	270	269	184	185	184	−435	−432	−426	−266	−264	−261	−182	−181	−179
65	191	196	179	125	123	104	86	84	71	−185	−161	−155	−106	−89	−86	−72	−61	−59
66	205	207	210	184	183	185	126	125	127	−75	−78	−81	−92	−95	−96	−63	−65	−65
67	9	6	6	91	67	61	62	46	42	−11	−4	−9	−111	−92	−90	−76	−63	−61
68	192	201	199	66	70	66	45	48	45	−169	−141	−147	−49	−40	−40	−34	−27	−28
69	353	332	336	202	190	194	138	130	133	−96	−81	−82	−50	−40	−39	−34	−27	−27
70	54	37	44	13	11	13	9	7	9	−51	−24	−34	−10	−4	−8	−7	−3	−5
min	3	1	1	1	1	1	1	0	0	−2	0	−1	−2	−1	−1	−1	−1	−1
max	658	661	673	395	395	401	270	270	274	−768	−780	−791	−509	−504	−509	−348	−345	−348
average	116	112	110	69	66	65	47	45	44	−122	−116	−114	−76	−72	−71	−52	−49	−48

Teeth modeled with cortical bone material properties (17 GPa). Values are in microstrain (με).
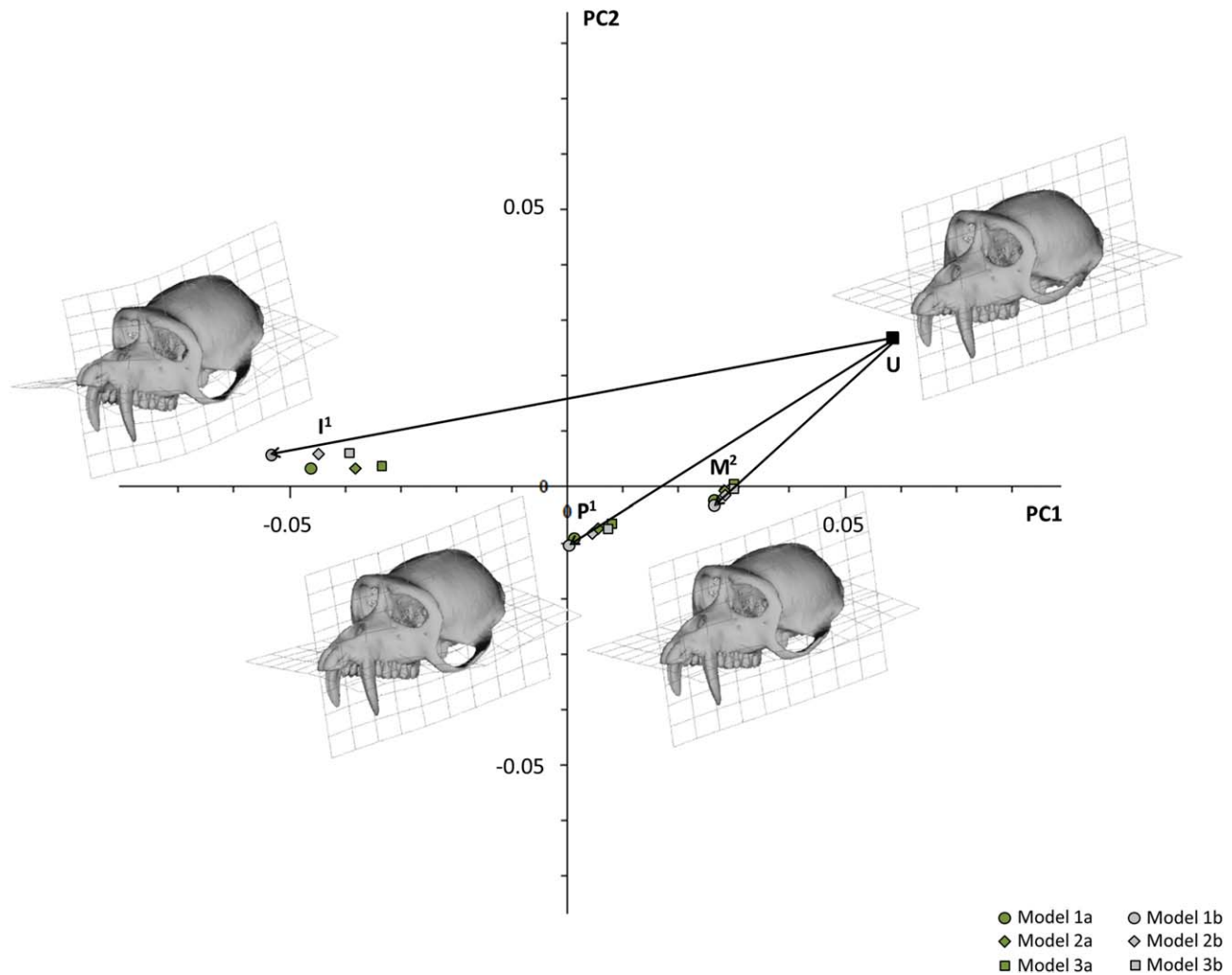
Fig. 6. The first principal component, PC1 (92.64% total variance) vs. the second principal component, PC2 (6.08%) from a principal components analysis of size and shape variables from 70 landmarks from each model during a 100 N bite at the three bite points. The square (U) represents the unloaded and thus undeformed *Macaca fascicularis* cranium, incisor (I[1]), premolar (P[1]), and molar (M[2]) bites represent the deformations due to biting on these specific teeth for each model. The different models are represented by the following symbols: circles = model 1 (original); diamonds = model 2 (trabecular bone and small cavities filled); squares = model 3 (model 2 plus maxillary sinus filled). Green symbols represent models with teeth modeled with dental material properties (models 1a, 2a, and 3a), while gray symbols represent models with teeth modeled with cortical bone material properties (model 1b, 2b, and 3b). The deformations are visualized using transformation grids and a deformed macaque surface. The grids are drawn vertically through the left zygomatic region and horizontally through the maxilla and cranial base. The reference specimen for the transformation grids is the undeformed model with the target specimens being I[1], P[1], and M[2] bites for model 1b; arrows are drawn between the reference and target models for each bite.

vs. 4). These differences are maximal at the alveolar margin, directly above the incisors and at the inferior margin of the nasal aperture (landmarks 1 and 2; ϵ3 increase of 105 με) when teeth are modeled as cortical bone. Strain also increases during premolar bites between models 1a and b, directly above the premolars, with ϵ3 increasing by 116 με (landmark 13; Tables 3 and 4), however, at most other landmarks, strain changes by only a few microstrain if at all. A similar effect is noted for molar bites when teeth are modeled as bone. Strains increase over the alveolar margin adjacent to the loaded tooth (landmarks 13–16 and 67; Tables 3 and 4) with the largest increase of 118 με at landmark 13, the inferior border of alveolar margin between the canine and P[1]. Some more distant regions, for example the maxillary

nasal region (landmarks 65 and 68), show an increase in strain >10 με during a M[2] bite, but in general, landmarks distant from the alveolus do not exhibit changes of more than a few με.

Assessment of Macaque Model Build Sensitivity Using Procrustes Size and Shape Analyses

The plot of PC1 (92% total variance) vs. PC2 (6%) from the size and shape PCA (Fig. 6) indicates that the most anterior bites most deform the cranium, with all models under I[1] load lying close together and furthest away from the unloaded cranium. The models under M[2] bite lie much closer to the unloaded model. The deformations under these different biting scenarios are

visualized for model 1b using warped surface models with superimposed transformation grids computed between the point representing the unloaded specimen and those representing I[1], P[1], and M[2] bites (Fig. 6) on this plot. With decreasing PC1 scores, there is increasing dorsoventral bending and an inferior deflection of the zygomatic arch. PC2 mainly relates to torsion within the rostrum with unilateral biting on P[1] producing the greatest degree and I[1] the least. Higher PCs show little of interest and account for 2% of total variance.

The six variants of each model (models 1a–3a,b; Fig. 6) form tight clusters according to loading condition (I[1] to M[2]). The incisor models show the greatest degree of variation. There are smaller differences among model variants in PC scores during molar bites. The differences due to tooth material properties are relatively small with the largest effect occurring during incisor biting simulations (Fig. 4). With increasing model filling (models 1–3), there is a decrease in overall cranial deformation, with the points representing model 2 (cancellous bone and foramina filled) and model 3 (maxillary sinus filled) falling progressively closer to the undeformed model in the plot. Points representing progressively filled models follow an almost linear trajectory over a short distance, indicating similar modes of, but progressively less, overall deformation. In addition, the greatest increases in stiffness are between models 1 and 2 irrespective of biting simulation or dental material properties. These findings are consistent with overall increases in stiffness of successively more solid models with the greatest increase occurring between models 1 and 2. The models cluster tightly according to load case rather than modeling approximation.

Macaque Model Sensitivity in Relation to Differences in Performance Between Species

To fully appreciate how variations in modeling parameters such as model segmentation and dental material properties might impact interpretation of comparative performance among closely related species, a comparably loaded model of *Cercocebus atys* (Fig. 7) with a simulated I[1] bite was included in a Procrustes size and shape analysis. PC1 explained 85.7% of the total variance while PC2 explained 8.9%. PC1 appears to be related to increased dorsovental bending, with increased bending occurring during more anterior loaded bites. The *Cercocebus* model with a simulated I[1] bite is widely separated from the loaded macaque models (Fig. 7). This indicates that the *Cercocebus* model deforms in a different way to the macaque model. The distance between the *Cercocebus* model with a simulated I[1] bite and the unloaded mean is smaller than the equivalent distance between the macaque models with simulated I[1] bites. This indicates that the *Cercocebus* model deforms less under incisor loading than does *Macaca*.

DISCUSSION

The use of simplified models is a necessity, particularly when dealing with fossils. While finite elements analysis is extensively used to compare the mechanical performance of skulls during biting, our understanding of how various model simplifications impact model performance is unclear. Such knowledge is particularly

important where FE modeling is used in comparative studies because the effects of model simplifications on cranial performance may be greater than the differences in performance among specimens or species. This study therefore examined the impact of modeling approximations on strains and global cranial deformations. These simplifications comprised sequential filling of the internal architecture of a macaque skull and alteration of the material properties of teeth. While these modeling assumptions are extreme they simulate simplifications that may need to be introduced in FEA, particularly when dealing with fossilized specimens.

Our findings indicate that ignoring the finer details of internal architecture, by making the model progressively more solid (filling cancellous and other small cavities with cortical bone), does not change the general distribution of surface strains but has noticeable localized effects, particularly in the maxillary region above the premolars. The biggest differences were recorded at the upper margin of each ear canal (porion). This reflects the filling of the mastoid air cells, ear canal and inner ear with cortical bone. The Procrustes size and shape analysis also demonstrates that the magnitude of large scale deformation of the skull decreases with increasing filling. This is unsurprising given the increased filling of the model with stiff material; however, the differences among models are significantly less than those among bites and the general modes of deformation are preserved.

Filling of the maxillary sinus in the model that was already largely filled had minimal further effects on the surface strain contours of the overlying maxilla, particularly during molar and premolar bites. The size and shape analysis shows a small decrease in large scale deformation, particularly during incisor bites. However, differences among models are moderate as compared to those among bites. These findings suggest that the maxillary sinus has little impact on facial stiffness in relation to biting. This is because it occupies a region of the facial skeleton that would otherwise experience low strains. This may be relevant to understanding the effects of facial loading on sinus morphogenesis and variation, and presents an interesting avenue of exploration for future FEA studies (O'Higgins et al., 2006, 2012). Parr et al. (2012) found a similar result in the mandible when cavities were filled. While they recorded slight decreases in bending displacements in their models with filled cavities, the pattern of strain distribution remained similar in the bone around the cavity.

With regard to the assignment of material properties, previous studies have noted that variations in bone material properties (Strait et al., 2005; Cox et al., 2011) and teeth (Cox et al., 2011) have a significant impact on strain magnitudes but not on the strain contours seen across the skull (Cox et al., 2011). The results of the present study indicate that allocating the same Young's modulus to teeth as to bone (17 GPa) does have an effect on local strain distributions close to the tooth itself. The largest increase in strain at any sampling point in this study was 118 $\mu\epsilon$, when the teeth were modeled with cortical bone and 100 N of bite force was applied. This was at the alveolus and the effect diminished markedly with distance from the alveolus. Similar localized effects in FE models of crania have been recorded in previous studies looking at the sensitivity of including or
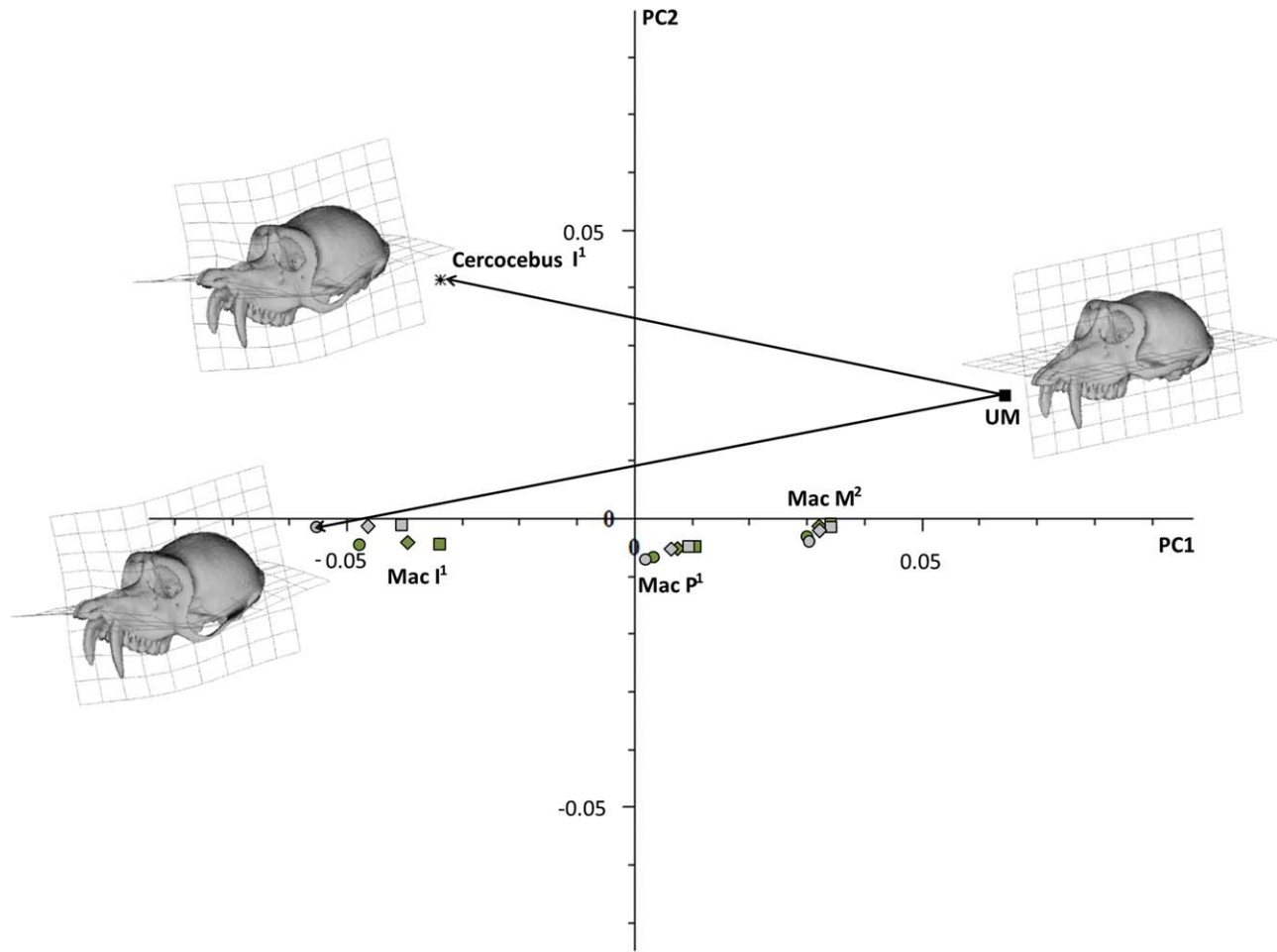
Fig. 7. The first principal component, PC1 (85.7% total variance) vs. the second principal component, PC2 (8.9%) from a principal components analysis of size and shape variables from 70 points during 100 N bites. *Macaca fascicularis* models (1a–3b) simulating incisor (I^1), premolar (P^1), and molar (M^2) bites and a *Cercocebus* model (comparable to macaque model 1a) simulating an I^1 bite. Macaque models have varying segmentation and dental material properties as described in the text and in the caption for Fig. 6. UM = undeformed mean; star = original *Cercocebus* model (teeth with bone material properties). The reference specimen for the transformation grids is the mean of the undeformed *Cercocebus* and macaque models with the target specimens being I^1 for *Cercocebus* and I^1 for the macaque model 1b. The UM surface is a macaque surface warped into the mean unloaded landmark configuration.

excluding representations of the periodontal ligaments by adding a collar of less stiff material between tooth and bone (Wood et al., 2011) and patent or fused cranial sutures (Kupczik et al., 2007; Wang et al., 2010; Bright, 2012; Wang et al., 2012) to the model. The degree of cranial deformation also increased slightly during incisor bites, compared to the postcanine bites, when teeth were modeled with the material properties of cortical bone rather than enamel. This increased dorsoventral bending is likely due to the alveolar region in the model becoming less stiff because the tooth roots, which lie deeply within the facial skeleton, are less stiff. This study indicates that changes in dental material properties will affect strain contours over the craniofacial skeleton, particularly near the teeth. This raises the need for caution in comparative FEAs as this is often a key area of interest (Strait et al., 2009). Differences in strains of similar order to those recorded here might be considered significant in comparable comparative studies.

In this study geometric morphometric techniques were employed to assess the sensitivity of FE models to simplifications in model building. Procrustes form analysis of large scale deformation has already been applied to sensitivity studies looking at the effects of various FE model parameters such as muscle loading (Cox et al., 2011; Fitton et al., 2012), material properties (Cox et al., 2011) and the PDL (Gröning et al., 2011). Here we more appropriately applied Procrustes size and shape analysis to investigate how the model simplifications impact global deformation, and analysed the results within a comparative framework. The six macaque models clustered tightly by bite point rather than by modeling simplification approach, and the deformations in *Cercocebus* are distinct from those in all macaque models. The similar but somewhat shorter trajectories of deformation recorded with increasing model solidification, particularly during the postcanine bites, indicate that more solid models become stiffer but show a less marked

difference in mode of deformation. Comparable findings were noted by O'Higgins and Milne (2013). Thus, the differences in deformation due to different modeling approaches are smaller than those due to the different bite points and much smaller than the differences in deformation between the *Cercocebus* and *Macaca* models during simulated incisor biting. GM appears to offer a useful additional tool for the examination of model sensitivity within FEA.

CONCLUSIONS

In summary, the present findings indicate that the macaque model subjected to simulated biting can be made solid with minimal impact on the large scale modes of deformation and resulting strain distributions. However, magnitudes of deformation are affected and there are localized effects on strain distributions. Certain locations exhibit moderate to large fluctuations in predicted strain magnitudes with different modeling approaches. Thus, filling of sinuses and other spaces impacts the prediction of strains over some localized regions of the face and cranium while altering the material properties of the teeth impacts more locally in the region of the alveolus. Such simplifications will affect predictions of fracture risk and remodeling in the affected regions. As such, model simplification needs to be undertaken with care and attention to its effects in the specific model and with regard to the question at hand. For questions concerning general aspects of the distribution of regions of relatively high or low strain and comparisons of large scale deformations, small errors in model reconstruction and certain simplifications of FE models will not unduly impact on findings. The size and shape analysis presented here allowed us to objectively compare the performance of different models with different sizes and shapes. We are currently gaining a greater understanding of the advantages and disadvantages of this approach (O'Higgins et al., 2011; Weber et al., 2011, O'Higgins and Milne, 2013) and of the relationship between Procrustes based methods and strain (Bookstein, 2013). More widely, however, it is as yet unclear how differences in local and global deformations from FEA relate to dietary ecology and other relevant parameters such as phylogeny (Daegling et al., 2013). A wider comparative study that takes account of within and between species variation as well as the effects of model simplification is needed to better clarify this issue. This current study raises the prospect that future applications of FEA to fossils with unknown internal architecture can produce reliable results with regard to general patterns of deformation, even when detail of internal bone architecture cannot be reliably modeled. It should be noted, however, that use of the modeling simplifications described here should, where possible, be supported by appropriate validation and sensitivity analyses.

ACKNOWLEDGEMENTS

LITERATURE CITED

Anapol F, Barry K. 1996. Fiber architecture of the extensors of the hindlimb in semiterrestrial and arboreal guenons. Am J Phys Anthropol 99:429–447.

Antón SC. 1999. Macaque Masseter muscle: internal architecture, fiber length and cross-sectional area. Int J Primatol 20:441–462.

Antón SC. 2000. Macaque pterygoid muscles: internal architecture, fiber length, and cross-sectional area. Int J Primatol 21:131–156.

Ashman RB, Van Buskirk WC. 1987. The elastic properties of a human mandible. Adv Dent Res 1:64–67.

Benazzi S, Bookstein FL, Strait DS, Weber GW. 2011. A new OH5 reconstruction with an assessment of its uncertainty. J Hum Evol 61:75–88.

Benazzi S, Kullmer Ottmar, Grosse IR, Weber GW. 2012. Brief communication: comparing loading scenarios in lower first molar supporting bone structure using 3D finite element analysis. Am J Phys Anthropol 147:128–134.

Benazzi S, Gruppioni G, Strait DS, Hublin JJ. 2014. Technical Note: Virtual reconstruction of KNM-ER 1813 *Homo habilis* cranium. Am J Phys Anthropol 153:154–160.

Bookstein FL. 1989. Principal warps: thin-plate splines and the decomposition of deformations. IEEE Trans Pattern Anal Mach Intell 11:567–585.

Bookstein FL. 2013. Allometry for the twenty-first century. Biol Theory 7:10–25.

Bright JA. 2012. The importance of craniofacial sutures in biomechanical finite element models in the domestic pig. PLOS One 7: e371769.

Chalk J, Richmond BG, Ross CF, Strait DS, Wright BW, Spencer MA, Wang Q, Dechow PC. 2011. A finite element analysis of masticatory stress hypotheses. Am J Phys Anthropol 145:1–10.

Cox PG, Fagan MJ, Rayfield EJ, Jeffery N. 2011. Finite element modelling of squirrel, guinea pig and rat skulls: using geometric morphometrics to assess sensitivity. J Anat 219:696–709.

Cox PG, Rayfield EJ, Fagan MJ, Herrel A, Pataky TC, Jeffery N. 2012. Functional evolution of the feeding system in rodents. PLOS One 7:1–11.

Curtis N, Jones M, Evans SE, O'Higgins P, Fagan MJ. 2010. Predicting muscle activation patterns from motion and anatomy: modelling the skull of Sphenodon (Diapsida: rhynchocephalia). J R Soc Interface 7:153–160.

Curtis N, Kupczik K, O'Higgins P, Moazen M, Fagan MJ. 2008. Predicting skull loading: applying multibody dynamics analysis to a macaque skull. Anat Rec 291:491–501.

Cuy JL, Mann AB, Livi KJ, Teaford MF, Weihs TP. 2002. Nanoindentation mapping of the mechanical properties of human molar tooth enamel. Arch Oral Biol 47:281–291.

Daegling DJ, Judex S, Ozcivici E, Ravosa MJ, Taylor AB, Grine FE, Teaford MF, Ungar PS. 2013. Viewpoints: feeding mechanics, diet, and dietary adaptations in early hominins. Am J Phys Anthropol 151:356–371.

Dechow PC, Nail GA, Schwartz-Dabney CL, Ashman RB. 1993. Elastic properties of human supraorbital and mandibular bone. Am J Phys Anthropol 90:291–306.

Demes B, Creel N. 1988. Bite force, diet, and cranial morphology of fossil hominids. J Hum Evol 17:657–670.

Dryden IL, Hirst JD, Melville JL. 2007. Statistical analysis of unlabelled point sets: comparing molecules in chemoinformatics. Biometrics 63:237–251.

Dumont ER, Davis JL, Grosse IR, Burrows AM. 2011. Finite element analysis of performance in the skulls of marmosets and tamarins. J Anat 218:151–162.

Dumont ER, Piccirillo J, Grosse IR. 2005. Finite-element analysis of biting behavior and bone stress in the facial skeletons of bats. Anat Rec Part 283A:319–330.

Fitton LC, Shi JF, Fagan MJ, O'Higgins P. 2012. Masticatory loadings and cranial deformation in *Macaca fascicularis*: a finite element analysis sensitivity study. J Anat 221:55–68.

Grine FE, Weber GW, Plavcan JM, Benazzi S. 2012. Sex at Sterkfontein: 'Mrs Ples' is still an adult female. J Hum Evol 62:593–604.

Gröning F, Fagan M, O'Higgins P. 2011. The effects of the periodontal ligament on mandibular stiffness: a study combining finite element analysis and geometric morphometrics. J Biomech 44:1304–1312.

Gunz P, Mitteroecker P, Neubauer S, Weber GW, Bookstein FL. 2009. Principles for the virtual reconstruction of hominin crania. J Hum Evol 57:48–62.

Heintz S, Gutierrez-Farewik EM. 2007. Static optimization of muscle forces during gait in comparison to EMG-to-force processing approach. Gait Posture 26: 279–288.

Jasinoski SC, Rayfield EJ, Chinsamy A. 2009. Comparative feeding biomechanics of *Lystrosaurus* and the generalised dicynodont *Oudenodon*. Anat Rec 292:862–874.

Kinney JH, Marshall SJ, Marshall GW. 2003. The mechanical properties of human dentin: a critical review and re-evaluation of the dental literature. Crit Rev Oral Biol Med 14:13–29.

Kupczik K, Dobson CA, Crompton RH, Phillips R, Oxnard CE, Fagan MJ, O'Higgins P. 2009. Masticatory loading and bone adaptation in the supraorbital torus of developing macaques. Am J Phys Anthropol 139:193–203.

Kupczik K, Dobson CA, Fagan MJ, Crompton RH, Oxnard CE, O'Higgins P. 2007. Assessing mechanical function of the zygomatic region in macaques: validation and sensitivity testing of finite element models. J Anat 210:41–53.

Macho GA, Shimizu D, Jiang Y, Spears IR. 2005. *Australopithecus anamensis*: a finite element approach to studying the functional adaptations of extinct hominins. Anat Rec Part A 283A:310–318.

McHenry CR, Clausen PD, Daniel WJT, Meers MB, Pendharkar A. 2006. Biomechanics of the rostrum in crocodilians: a comparative analysis using finite element modeling. Anat Rec 288A:827–849.

Milne N and O'Higgins P. 2012. Scaling of form and function in the xenarthran femur: a 100-fold increase in body mass is mitigated by repositioning of the third trochanter. Proc R Soc B 279:3449–3456.

Mitteroecker P, Gunz P, Bernhard M, Schaefer K, Bookstein FL. 2004. Comparison of cranial ontogenetic trajectories among great apes and humans. J Hum Evol 46:679–698.

O'Higgins P, Cobb SN, Fitton LC, Gröning F, Philips R, Liu J, Fagan M. 2011. Combining geometric morphometrics and functional simulation: an emerging toolkit for virtual functional analyses. J Anat 218:3–15.

O'Higgins P, Fitton L, Phillips R, Shi JF, Liu J, Gröning F, Cobb SN, Fagan MJ. 2012. Virtual functional morphology: novel approaches to the study of craniofacial form and function. Evol Biol 39:521–535.

O'Higgins P, Milne N. 2013. Applying geometric morphometrics to compare changes in size and shape arising from finite elements analyses. Hystrix Ital J Mammal 24:136–132.

Parr WCH, Wroe S, Chamoli U, Richards HS, McCurry MR, Clausen PD, McHenry C. 2012. Toward integration of geometrics

morphometrics and computational biomechanics: new methods for 3D virtual reconstruction and quantitative analysis of finite element models. J Theor Biol 301:1–14.

Rasmussen J, Voigt M. 2001. Muscle recruitment by the min/max criterion—a comparative numerical study. J Biomech 34:409–415.

Ross CF, Patel BA, Slice DE, Strait DS, Dechow PC, Richmond BG, Spencer MA. 2005. Modeling masticatory muscle force in finite element analysis: sensitivity analysis using principal coordinates analysis. Anat Rec 283A:288–299.

Shi J, Curtis N, Fitton LC, O'Higgins P, Fagan M. 2012. Developing a musculoskeletal model of the primate skull: predicting muscle activations, bite force and joint reaction forces using multibody dynamics analysis and advanced optimisation methods. J Theor Biol 310:21–30.

Strait DS, Constantino P, Lucas PW, Richmond BG, Spencer MA, Dechow PC, Ross CF, Grosse IR, Wright BW, Wood BA, Weber GW, Wang Q, Byron C, Slice DE, Chalk J, Smith AL, Smith LC, Wood S, Berthaume M, Benazzi S, Dzialo C, Tamvada K, Ledogar JA. 2013. Viewpoints: diet and dietary adaptations in early hominins: the hard food perspective. Am J Phys Anthropol 151:339–355.

Strait DS, Grosse IR, Dechow PC, Smith AL, Wang Q, Weber GW, Neubauer S, Slice DE, Chalk J, Richmond BG, Lucas PW, Spencer MA, Schrein C, Wright BW, Byron C, Ross CF. 2010. The structural rigidity of the cranium of *Australopithecus africanus*: implications for diet, dietary adaptations and the allometry of feeding biomechanics. Anat Rec 293:583–593.

Strait DS, Richmond BG, Spencer M A, Ross CF, Dechow PC, Wood BA (2007) Masticatory biomechanics and its relevance to early hominid phylogeny: an examination of palatal thickness using finite-element analysis. J Hum Evol 52:585–599.

Strait DS, Wang Q, Dechow PC, Ross CF, Richmond BG, Spencer MA, Patel BA. 2005. Modeling elastic properties in finite-element analysis: how much precision is needed to produce an accurate model? Anat Rec 283A:275–287.

Strait DS, Weber GW, Neubauer S, Chalk J, Richmond BG, Lucas PW, Spencer MA, Schrein C, Dechow PC, Ross CF, Grosse IR, Wright BW, Constantino P, Wood BA, Lawn B, Hylander WL, Wang Q, Byron C, Slice DE, Smith AL. 2009. The feeding biomechanics and dietary ecology of *Australopithecus africanus*. PNAS 106:2124–2129.

Wang Q, Smith AL, Strait DS, Wright BW, Richmond BG, Grosse IR, Byron CD, Zapata U. 2010. The global impact of sutures assessed in a finite element model of a macaque cranium. Anat Rec 293:1477–1491.

Wang Q, Wood SA, Grosse IR, Ross CF, Zapata U, Byron CD, Wright BW, Strait DS. 2012. The role of sutures in biomechanical dynamic simulation of a macaque cranial finite element model: implications for the evolution of craniofacial form. Anat Rec 295:278–288.

Weber GW, Bookstein FL, Strait DS. 2011. Virtual anthropology meets biomechanics. J Biomech 44:1429–1432.

Weijs WA, Hillen B. 1985. Cross-sectional areas and estimated intrinsic strength of the human jaw muscles. Acta Morphol Neerl Scand 23:267–274.

Wood SA, Strait DS, Dumont ER, Ross CF, Grosse IR. 2011. The effect of modeling simplifications on craniofacial finite element models: the alveoli (tooth sockets) and periodontal ligaments. J Biomech 44:1831–1838.

Wroe S, Clausen P, McHenry C, Moreno K, Cunningham E. 2007. Computer simulation of feeding behaviour in the thylacine and dingo as a novel test for convergence and niche overlap. Proc R Soc B 274:2819–2828.

Wroe S, Ferrara TL, McHenry CR, Curnoe D, Chamoli U. 2010. The craniomandibular mechanics of being human. Proc R Soc B 277: 3579–3586.